PHYSICAL REVIEW A **107**, 033519 (2023)

Editors' Suggestion

Static and dynamic properties of self-bound droplets of light in hot vapors

Heitor da Silva,[1,2] Robin Kaiser,[2] and Tommaso Macrì[1,3]
[1]*Departamento de Física Teórica e Experimental, Universidade Federal do Rio Grande do Norte, 59072-970 Natal, Rio Grande do Norte, Brazil*
[2]*Institut de Physique de Nice, CNRS, Université Côte d'Azur, 06560 Valbonne, France*
[3]*ITAMP, Harvard-Smithsonian Center for Astrophysics, Cambridge, Massachusetts 02138, USA*

(Received 20 November 2022; accepted 16 March 2023; published 24 March 2023)

The propagation of light in nonlinear media is well described by a two-dimensional nonlinear Schrödinger equation (NLSE) within the paraxial approximation, which is equivalent to the Gross-Pitaevskii equation, the mean-field description for the dynamics of Bose-Einstein condensates (BECs). Due to this similarity, many theoretical and experimental investigations of phenomena which have already been studied and realized in BECs have been recently analyzed in alternative experimental platforms such as hot atomic vapors. In this work we study the formation of droplets of light in these media, attempting to establish a mapping between the experimental parameters normally used in BEC experiments and those needed to observe the analogous phenomenon in hot atomic vapors. We obtain the energy functional for the susceptibility of the medium in the $\chi^{(3)}$, $\chi^{(3)}+\chi^{(5)}$, and saturating regimes for a two-level atomic configuration considering the focusing (attractive) regime. We apply a Gaussian variational approach and check its predictions through numerical simulations of the NLSE for each regime. Finally, we study the real-time dynamics of the system for both the $\chi^{(3)}+\chi^{(5)}$ and saturating nonlinearities, focusing our attention on the behavior of the breathing mode and on the analysis of droplet formation for realistic experimental conditions.

DOI: 10.1103/PhysRevA.107.033519

I. INTRODUCTION

The field of atomic physics has achieved great advances over the decades, especially due to the progress seen on the experimental side. The advances obtained with experiments using ultracold atoms have made it possible to investigate many phenomena in various branches of physics. However, such experiments may bring with them some obstacles depending on the physical phenomenon one wants to study as well as their costs, which can be much higher when compared to other experimental platforms. For instance, there are many phenomena observed in Bose-Einstein condensates (BECs) which have been investigated recently on alternative platforms such as hot atomic vapors [1,2]. A hot vapor is an extremely versatile experimental platform and it has been the workhorse in atomic physics over the years. What makes this transition possible is the existing analogy between the mean-field description for BECs, which is given by the Gross-Pitaevskii equation, and the equation for propagation of light in a nonlinear medium in the paraxial approximation, an example of a nonlinear Schrödinger equation (NLSE). With that, one can then attempt to establish a mapping between the experimental parameters of the condensates and those of the thermal vapors. In fact, this analogy has already been exploited in several theoretical and experimental works (using thermal vapors) including condensation of classical waves [3–5], superfluidity of a paraxial fluid of light [6–8], vortex generation and control of their interactions [9], the generation and the dynamics of dispersive shock and blast waves [10–15], spin-orbit-coupled mixtures [16], and even the investigation of analog models in gravity, for instance, the analog of cosmological particle creation [17]. When compared to ultracold experiments, one of the advantages of thermal vapors is that they are relatively cheap and much simpler to set up. Another advantage is revealed when there is the need to obtain higher densities. Since the susceptibility of a nonlinear medium depends on the density of the medium, the use of a thermal vapor helps one attain higher densities. In ultracold experiments, typical densities vary in the range 10^{11}–10^{12} cm^{-3} in a magneto-optical trap, while in a BEC they range from 10^{13} to 10^{15} cm^{-3}. Meanwhile, hot atomic vapors can have densities orders of magnitude larger than BECs and are tunable over a much wider range.

The purpose of this work is to characterize self-bound states of light in hot vapors, in analogy to droplet states in binary mixtures of BECs and dipolar systems. Quantum droplets consist of small clusters of atoms, self-bounded by the balance of an attractive mean-field energy and repulsive beyond mean-field interactions [18]. Several experiments have successfully observed ultradilute self-bound states in a variety of configurations such as ultracold dipolar systems [19,20], Bose-Bose mixtures in quasi-2D and quasi-1D geometries [21,22], and 3D geometry [23], among others.

In this study we consider a nonlinear hot vapor medium modeled as an ensemble of two-level systems. Our target is the focusing (attractive) regime. The physical parameter that sets the sign of the interaction is the frequency detuning. We investigate three different regimes: a Kerr medium, i.e., the refractive index has a linear dependence on the intensity; the cubic-quintic nonlinearity, that is, up to second order in the intensity; and finally, the most general saturating nonlinearity. For each of these situations, we analyze the corresponding

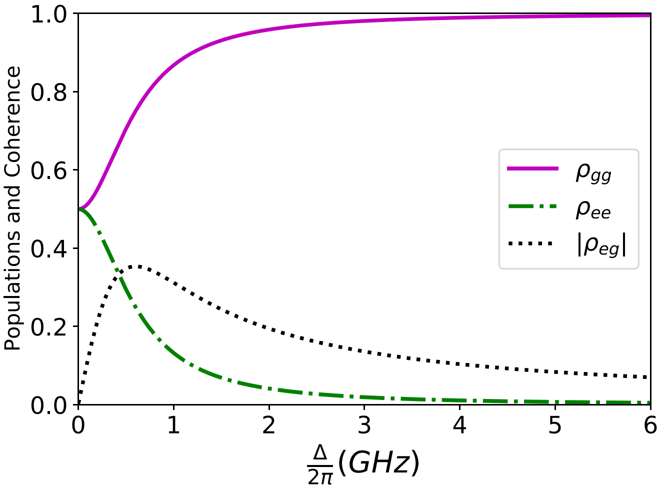

FIG. 1. Atomic level description. Stationary populations and coherence for the two-level system as a function of the frequency detuning Δ.

energy functional. For this task, we will make use of a variational approximation method and exact numerical simulations [24–28].

This paper is organized as follows. In Sec. II we derive the effective NLSE for light propagating through an ensemble of two-level systems with susceptibility χ. In Sec. III we compute the energy functionals employing a variational Gaussian ansatz. In Sec. IV we address the real-time dynamics. We briefly analyze the $\chi^{(3)}$ regime, focusing on the physics of the Townes soliton and commenting on its main features (Sec. IV A). We proceed with the study of collective excitations (the breathing mode), defining the range of parameters for which they can be observed (Sec. IV B). Also, we establish a connection with the self-evaporation mechanism and its influence on droplet dynamic formation within the $\chi^{(3)} + \chi^{(5)}$ and saturating regimes. Finally, we study the droplet formation for realistic experimental conditions (Sec. IV C). We summarize in Sec. V.

II. PHYSICAL SYSTEM

We consider an ensemble of two-level systems formed by a ground state $|g\rangle$ and an excited state $|e\rangle$ that can decay into the ground state at a rate Γ. The optical Bloch equations (OBEs) for this configuration are easily obtained and their steady-state solutions for the populations and the coherence are shown in Fig. 1 (see Appendix A for the full expressions).

The susceptibility is given by

$$\chi = \frac{\rho_{\text{at}}|\mathbf{d}_{eg}|^2}{\hbar\epsilon_0}\frac{-\Delta + i\Gamma/2}{\Delta^2 + \frac{\Gamma^2}{4} + \frac{|\Omega|^2}{2}}, \tag{1}$$

where ρ_{at} is the atom density and $\hbar\Omega = -\mathbf{d}_{eg}\cdot\mathbf{E}$ is the Rabi frequency, with $\mathbf{E}$ the classical external electric field. In this expression, Re[χ] represents the refractive index of the medium, while Im[χ] is responsible for the absorption. Our model is a simplified description of the system. In the region close to the resonance, absorption, collisional, and thermal effects due the Doppler broadening might play an important role in the dynamics of the system. However, for sufficiently high values of the frequency detuning Δ, such effects turn out to be negligible. For instance, in the low-saturation regime, we can provide an estimate of absorption effects by computing the ratio $|\text{Im}[\chi]/\text{Re}[\chi]|$. For $\Delta = 2\pi \times 1.0$ GHz and for the case of ^{85}Rb whose natural linewidth is equal to $\Gamma = 2\pi \times 6.06$ MHz for the $D2$ line, a direct calculation gives $|\text{Im}[\chi]/\text{Re}[\chi]| \sim 3\times 10^{-3}$. Therefore, our analysis and results shown hereafter will be relevant for large values of the frequency detuning.

The linear real susceptibility $\chi^{(L)}$ reads

$$\chi^{(L)} = -\frac{\rho_{\text{at}}|\mathbf{d}_{eg}|^2}{\hbar\epsilon_0}\frac{\Delta}{\Delta^2 + \frac{\Gamma^2}{4}}, \tag{2}$$

while the real nonlinear part of the full susceptibility is obtained after subtracting $\chi^{(L)}$ and taking the real part, yielding

$$\chi^{(\text{NL})} = \frac{\rho_{\text{at}}|\mathbf{d}_{eg}|^2}{\hbar\epsilon_0}\frac{\Delta|\Omega|^2/2}{\left(\Delta^2 + \frac{\Gamma^2}{4}\right)\left(\Delta^2 + \frac{\Gamma^2}{4} + \frac{|\Omega|^2}{2}\right)}. \tag{3}$$

In the paraxial approximation, the NLSE for the light field amplitude is given by

$$i\frac{\partial\Omega}{\partial z} = -\frac{1}{2k_0}\nabla_\perp^2\Omega - \frac{k_0}{2}\chi\Omega. \tag{4}$$

In this equation, the longitudinal coordinate z plays the role of an effective time, while the Laplacian is computed with respect to the transverse coordinates, i.e., $\mathbf{r} \equiv (x, y)$, and k_0 is the wave vector.

Performing the transformation

$$\bar{\Omega}(\mathbf{r}, z) = \Omega(\mathbf{r}, z)\exp\left(-i\frac{k_0\chi^{(L)}}{2}z\right), \tag{5}$$

we are left with the equation

$$i\frac{\partial\Omega}{\partial z} = -\frac{1}{2k_0}\nabla_\perp^2\Omega - \frac{k_0}{2}\chi^{(NL)}\Omega. \tag{6}$$

This equation can be written in a dimensionless form by performing the scalings

$$\mathbf{r}' = \frac{\mathbf{r}}{r_0}, \quad z' = \frac{z}{L_d}, \quad \psi = \alpha\Omega, \tag{7}$$

where r_0 is an arbitrary length scale, $L_d(r_0) = k_0 r_0^2$ is the associated diffraction length, and α is a parameter depending on the optical parameters whose dimension is the inverse frequency [see Eq. (9a)]. Later on, for the numerical simulations, we will consider a Gaussian input beam by setting $r_0 = w_0$, where w_0 is the initial beam waist [29], for which the Rayleigh length is defined as $z_R = \frac{1}{2}L_d(w_0)$.

The dimensionless equation of motion then reads

$$i\frac{\partial\psi}{\partial z'} = -\frac{1}{2}\nabla_\perp'^2\psi - \frac{1}{1 + 2\gamma|\psi|^2}|\psi|^2\psi, \tag{8}$$

where ψ is the scaled light field amplitude. The Laplacian now has to be computed with respect to the dimensionless transverse coordinates, i.e., $\mathbf{r}' \equiv (x', y')$. It is straightforward to check that, for $\gamma|\psi|^2 \ll 1$, a series expansion of the nonlinear term in Eq. (8) in $|\psi|^2$ will lead to the cubic NLSE (Kerr medium) in zeroth order and to the cubic-quintic NLSE up to first order.

The parameter α in Eq. (7) is related to the strength of the nonlinearity of the system. It is also connected to the dimensionless critical optical power $\mathcal{P}_{\text{cr}}$, a quantity that will be important to classify the regimes for which self-bound state solutions and collapsing behavior occur. For a description beyond the Kerr regime, α will no longer be the only interaction parameter. This role will be shared with the dimensionless parameter γ, responsible for turning on the terms beyond the cubic NLSE.

The parameters α and γ take on the expressions

$$\alpha = \frac{k_0 r_0}{2\Gamma}\sqrt{\eta\frac{\Delta/\Gamma}{\left[\left(\frac{\Delta}{\Gamma}\right)^2+\frac{1}{4}\right]^2}}, \tag{9a}$$

$$\gamma = \left[(k_0 r_0)^2\eta\frac{\Delta/\Gamma}{\left(\frac{\Delta}{\Gamma}\right)^2+\frac{1}{4}}\right]^{-1}, \tag{9b}$$

where Γ is the natural linewidth and the dimensionless coefficient η is related to the density and consequently to the temperature of the atomic cloud [30]. Its expression is given by

$$\eta = \frac{\rho_{\text{at}}|\mathbf{d}_{eg}|^2}{\hbar\epsilon_0\Gamma}, \tag{10}$$

where $\mathbf{d}_{eg}$ is the transition dipole moment between the ground-state manifold g and the excited-state manifold e. Alternatively, η can be rewritten in terms of the wavelength λ employing the spontaneous emission rate Γ in vacuum, reading [31]

$$\Gamma = \frac{\omega_0^3}{3\pi\epsilon_0\hbar c^3}|\mathbf{d}_{eg}|^2,$$

which leads to

$$\eta = \frac{3\rho_{\text{at}}\lambda^3}{8\pi^2}. \tag{11}$$

The parameter α can be recast to include negative values of Δ by taking the absolute value and flipping the global sign of the nonlinear interaction term in Eq. (8). In our numerical analysis, the values for the quantities were chosen to consider the specific case of a thermal vapor of ^{85}Rb whose natural linewidth is $\Gamma = 2\pi \times 6.06$ MHz for the $D2$ line ($5\,^2S_{1/2} \rightarrow 5\,^2P_{3/2}$ transition). By considering a π-polarized light, it follows that the value of the effective far-detuned dipole moment is 2.069×10^{-29} C m while the saturation intensity is equal to 25 W/m^2 [30].

III. ENERGY FUNCTIONALS AND THE GAUSSIAN VARIATIONAL ANSATZ

In this section we study the stationary properties of the system by means of the analysis of the energy functionals describing stationary configurations. From the general saturating nonlinearity, we derive the energy functional for the $\chi^{(3)}$ and $\chi^{(3)}+\chi^{(5)}$ regimes upon Taylor expansion in the parameter $\gamma|\psi|^2$. We then evaluate the resulting expressions using a Gaussian ansatz for the dimensionless light field amplitude ψ. The use of a variational approach allows us to derive analytical results to assess the static and dynamic behaviors of the system close to the stationary configurations, similar to the case of BECs [28,32].

A. Energy functionals

The energy functional for the saturating regime, here denoted by $E^{(\text{sat})}$, can be obtained directly from Eq. (8), which yields

$$E^{(\text{sat})} = \frac{1}{2}\int|\nabla'_\perp\psi(\mathbf{r}')|^2 d^2\mathbf{r}' - \frac{1}{2\gamma}\int|\psi(\mathbf{r}')|^2 d^2\mathbf{r}' + \frac{1}{4\gamma^2}\int\ln[1+2\gamma|\psi(\mathbf{r}')|^2]d^2\mathbf{r}'. \tag{12}$$

We start by considering the Gaussian input profile [33–35]

$$\psi(\mathbf{r}') = \sqrt{\frac{\mathcal{P}}{\pi\sigma'^2}}\exp\left(-\frac{r'^2}{2\sigma'^2}\right), \tag{13}$$

where the dimensionless width $\sigma' = \sigma/r_0$ is the variational parameter and $\mathcal{P}$ is the dimensionless power which depends on the optical parameters of the system through α [see Eq. (7)]. Although r_0 is among the parameters contained in the definition of α, the values of the physical quantities will be independent of its choice.

We compute $E^{(\text{sat})}$ using the ansatz given in Eq. (13), which yields

$$E^{(\text{sat})} = \frac{1}{2\sigma'^2}\mathcal{P} - \frac{1}{2\gamma}\mathcal{P} - \frac{\pi}{4\gamma^2}\sigma'^2\text{Li}_2\left(-\frac{2\gamma}{\pi\sigma'^2}\mathcal{P}\right), \tag{14}$$

where $\text{Li}_2(x)$ is the polylogarithmic function of order 2. For $\gamma|\psi|^2 \ll 1$, we can perform a Taylor expansion in the logarithmic term of Eq. (12). Truncation to the first order produces the $\chi^{(3)}$ regime, whereas the second order leads to the $\chi^{(3)}+\chi^{(5)}$ regime. The expressions for $E^{(3)}$ and $E^{(5)}$ are

$$E^{(3)} = \frac{1}{2}\int|\nabla'_\perp\psi(\mathbf{r}',z')|^2 d^2\mathbf{r}' - \frac{1}{2}\int|\psi(\mathbf{r}',z')|^4 d^2\mathbf{r}', \tag{15a}$$

$$E^{(5)} = \frac{1}{2}\int|\nabla'_\perp\psi(\mathbf{r}',z')|^2 d^2\mathbf{r}' - \frac{1}{2}\int|\psi(\mathbf{r}',z')|^4 d^2\mathbf{r}' + \frac{2\gamma}{3}\int|\psi(\mathbf{r}',z')|^6 d^2\mathbf{r}'. \tag{15b}$$

Employing the Gaussian ansatz from Eq. (13), we obtain

$$E^{(3)} = \frac{1}{2\sigma'^2}\mathcal{P} - \frac{1}{4\pi\sigma'^2}\mathcal{P}^2, \tag{16a}$$

$$E^{(5)} = \frac{1}{2\sigma'^2}\mathcal{P} - \frac{1}{4\pi\sigma'^2}\mathcal{P}^2 + \frac{2\gamma}{9\pi^2\sigma'^4}\mathcal{P}^3. \tag{16b}$$

B. Cubic-quintic nonlinearity $\chi^{(3)}+\chi^{(5)}$

We now analyze the cubic-quintic nonlinearity. The expansion of Eq. (8) up to first order in $\gamma|\psi|^2 \ll 1$ leads to

$$i\frac{\partial\psi}{\partial z'} = -\frac{1}{2}\nabla'^2_\perp\psi - |\psi|^2\psi + 2\gamma|\psi|^4\psi. \tag{17}$$

The $\chi^{(3)}+\chi^{(5)}$ regime provides the suitable conditions for creating self-bound states due to the competition between

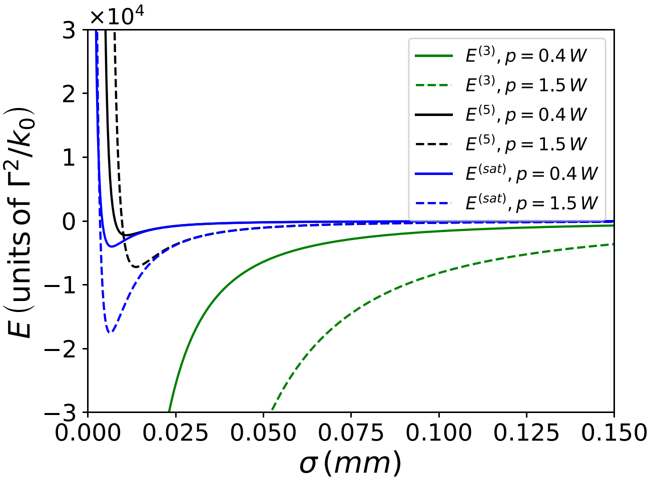

FIG. 2. Variational approach to the ground state. Energy is computed for the $\chi^{(3)}$ (green), $\chi^{(3)} + \chi^{(5)}$ (black), and saturating (blue) regimes for $p = 0.4$ (solid lines) and 1.5 W (dashed lines), and the frequency detuning equal to $\Delta = 2\pi \times 3.0$ GHz.

the focusing (attractive) $\chi^{(3)}$ and defocusing (repulsive) $\chi^{(5)}$ nonlinearities [36–38]. The conditions leading to self-bound states of light were pointed out in [39]. There it was shown that for a four-level system, an adequate choice of the parameters for an electromagnetic-induced transparency scheme may lead to a giant response for the coefficients of both the cubic and quintic nonlinearities (with different signs) stabilizing two-dimensional droplets. More recently, it was shown that bound states with finite angular momentum with liquidlike properties can arise when considering a nonlocal photon fluid with a focusing long-range nonlinearity generated in the transverse plane of a laser beam propagating in a thermo-optic medium [40,41].

We start with the analysis of the energy functional $E^{(5)}$ given in Eq. (16b). Setting its derivative with respect to σ' to zero leads to

$$\sigma'_c = \frac{4\mathcal{P}\sqrt{\gamma}}{3\sqrt{\pi}\sqrt{-2\pi + \mathcal{P}}}, \tag{18}$$

where $\mathcal{P} > 2\pi$ must be satisfied. By taking the second derivative $d^2E^{(5)}/d\sigma'^2$ at $\sigma' = \sigma'_c$, we can show that Eq. (18) is a minimum. Moreover, this is a global minimum, since the energy is negative at $\sigma' = \sigma'_c$, excluding the presence of metastable minima.

C. Saturating nonlinearity

Stable self-bound states for the saturating regime were investigated, for instance, in [42,43]. For the saturating regime, an analytical expression for the stationary value σ' is not available. For the parameters used in the simulations and in most analysis throughout this work (unless specifically stated otherwise), we set the beam waist w_0 equal to 7×10^{-4} m and the coefficient η to unity, leading to an atom density of $\rho_{\text{at}} = 8.30 \times 10^{19}$ m^{-3}.

In Fig. 2 we show the energy as a function of σ for the $\chi^{(3)}$, $\chi^{(3)} + \chi^{(5)}$, and saturating regimes for two different values of the incident power p and $\Delta = 2\pi \times 3.0$ GHz. We observe that the energy displays a minimum for the $\chi^{(3)} + \chi^{(5)}$ and saturating regimes for a wide range of powers. Similarly, the $\chi^{(3)}$ curves do not hold a minimum: The energy either decreases or increases indefinitely, depending on whether the focusing term dominates or the diffraction (kinetic) takes over, respectively. Notwithstanding, for very high values of Δ the nonlinearity becomes irrelevant when compared to diffraction for all regimes.

Next, we investigate the values of the width $\sigma_r(z) = \sqrt{\langle r^2\rangle - \langle r\rangle^2}$, a quantity that provides an estimate of the droplet's radius σ. We then run numerical simulations of Eqs. (8) and (17) using imaginary-time evolution to reach the minimum energy state.

Figure 3 shows a comparison between the variational approach and the numerical results. There is an upper limit for Δ once the incident power p is chosen, which follows from the constraint over the values of $\mathcal{P}$ in Eq. (18). Concurrently, increasing Δ makes the nonlinearity weaker, so the droplet states will not be sustained. The rectangular gray regions in the plots display the forbidden range of values for Δ. For $p = 0.4$ W, the upper limit is for $\Delta \approx 2\pi \times 6.0$ GHz, while for $p = 1.5$ W, the limiting value is $2\pi \times 9.6$ GHz (magenta dashed lines).

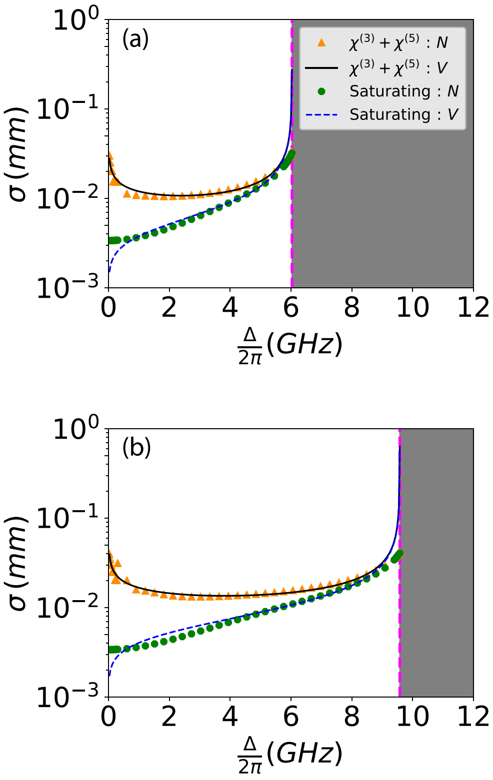

FIG. 3. The rms deviation of the radial position as a function of the frequency detuning Δ. The values of the incident powers are (a) $p = 0.4$ and (b) $p = 1.5$ W. The curves with markers refer to the numerical results (N) obtained from the NLSE: orange triangles for the $\chi^{(3)} + \chi^{(5)}$ regime and green octagons for the saturating regime. For the variational results (V), the black solid curve represents the $\chi^{(3)} + \chi^{(5)}$ regime, while the blue dashed line shows the results obtained for the saturating regime.

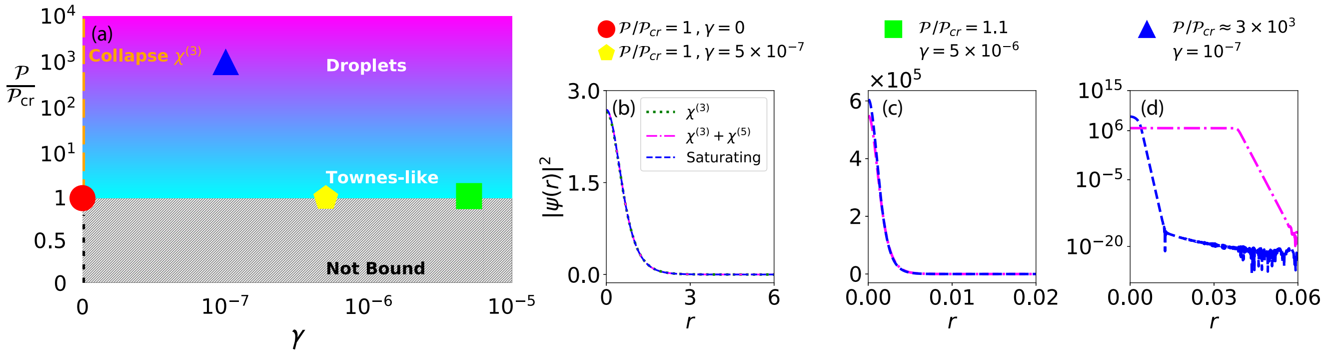

FIG. 4. Ground state of the system. (a) Phase diagram. After an interval in which diffraction dominates over the nonlinear interaction (not bound region), from cyan to magenta, one transits from the weakly nonlinear regime (Townes soliton) to the strong nonlinear regime (droplets). For the pure $\chi^{(3)}$ regime (green dotted line), if $\mathcal{P}/\mathcal{P}_{\rm cr} > 1$ then one enters the collapsing region as pictured by the orange dotted line for $\gamma = 0$. When considering the $\chi^{(3)} + \chi^{(5)}$ (magenta dash-dotted lines) and saturating regimes (blue dashed lines), for any $\gamma > 0$, the collapse is arrested. Also shown are the intensity profiles $|\psi(\mathbf{r})|^2$ for different values of the ratio $\mathcal{P}/\mathcal{P}_{\rm cr}$ and γ: (b) $\mathcal{P}/\mathcal{P}_{\rm cr} = 1$ and $\gamma = 0$ (red circle) and $\gamma = 5 \times 10^{-7}$ (yellow pentagon), (c) $\mathcal{P}/\mathcal{P}_{\rm cr} = 1.1$ and $\gamma = 5 \times 10^{-6}$ (green square), and (d) $\mathcal{P}/\mathcal{P}_{\rm cr} \approx 3 \times 10^3$ and $\gamma = 10^{-7}$ (blue triangle).

These results reveal good agreement between the values obtained through the variational Gaussian ansatz and those obtained from the numerical simulations of Eqs. (8) and (17). We see that the values for σ in the $\chi^{(3)} + \chi^{(5)}$ and saturating regimes will converge for a wide range of increasing values of the frequency detuning, except close to the lower and upper bounds. In these two regions, we observe that the beam cannot be approximated by a Gaussian profile and therefore we expect a disagreement between the numerical and variational results.

D. Ground-state phase diagram

We now investigate the phase diagram of the system. We run numerical simulations in imaginary time for the different regimes. The results obtained for the intensity profiles (here considering the dimensionless quantities) are shown in Fig. 4.

In two dimensions, it is known that the focusing cubic NLSE admits the Townes solution for a specific value of the dimensionless power that we here denote by $\mathcal{P}_{\rm cr}$, which equals $\mathcal{P}_{\rm cr} = 5.8504$ [29,44]. The Townes soliton is only one of the stationary solutions that this equation possesses. Higher-order stationary solutions (all of them with $E = 0$, like the Townes soliton) will present nodes in addition to having an associated power greater than $\mathcal{P}_{\rm cr}$ [45,46]. For values of the dimensionless power smaller than $\mathcal{P}_{\rm cr}$, the nonlinear interaction is too weak and thus the contribution of the transverse Laplacian dominates, leading to a spreading of the intensity profile. In the phase diagram, this situation corresponds to the gray shaded region and it is valid for any value of γ (the black dotted line corresponds to $\gamma = 0$, that is, the pure Kerr nonlinearity). As $\mathcal{P}$ slightly increases, we eventually reach the critical value for the Townes solution, $\mathcal{P} = \mathcal{P}_{\rm cr}$. This point is represented by the red circle in the phase diagram and by the green dotted line in Fig. 4(b). At this point we have $\mathcal{P}/\mathcal{P}_{\rm cr} = 1$ and $\gamma = 0$. (Further details on the physics of the Townes soliton will be discussed in Sec. IV.) For the yellow pentagon, the higher-order nonlinear terms are still irrelevant when compared to the leading-order $\chi^{(3)}$ interaction and the intensity profiles remain the same as seen in Fig. 4(b). However, this picture dramatically changes when the ratio $\mathcal{P}/\mathcal{P}_{\rm cr}$ increases. In this case, the NLSE containing only the Kerr term will lead to collapsing solutions, which is indicated in the phase diagram by the vertical orange dotted line along $\gamma = 0$. When considering the other regimes (which corresponds to the green square), this collapse is arrested and stable configurations can be obtained, as shown in Fig. 4(c) for the $\chi^{(3)} + \chi^{(5)}$ (magenta dash-dotted line) and saturating regimes (blue dashed line), although the intensity profiles are practically equal for these two situations. For this collapsing region, we did not represent the $\chi^{(3)}$ regime because it would require an extremely fine spatial grid. Here the system suffers a very strong focusing effect, so the peak intensity takes on very high values, which characterizes the collapsing behavior. By considering even higher values of the dimensionless power, we start seeing some differences between the $\chi^{(3)} + \chi^{(5)}$ and saturating regimes. The nonlinearity gets stronger closer to resonance, and concomitantly, we eventually see the formation of flat-top profiles for the $\chi^{(3)} + \chi^{(5)}$ regime while its saturating counterpart displays a Gaussian-like shape as shown in Fig. 4(d).

IV. REAL-TIME DYNAMICS: GENERAL ASPECTS, BREATHING MODE, AND REALISTIC EXPERIMENTAL CONDITIONS

In this section we investigate the real-time dynamics of a Gaussian beam for the nonlinearities presented above. In Sec. IV A we review the real-time dynamics for the $\chi^{(3)}$ regime and comment on the physics of the Townes soliton. We proceed in Secs. IV B and IV C with the investigation of the breathing mode and the real-time dynamics for a Gaussian beam under realistic experimental conditions for both the $\chi^{(3)} + \chi^{(5)}$ and saturating regimes, respectively.

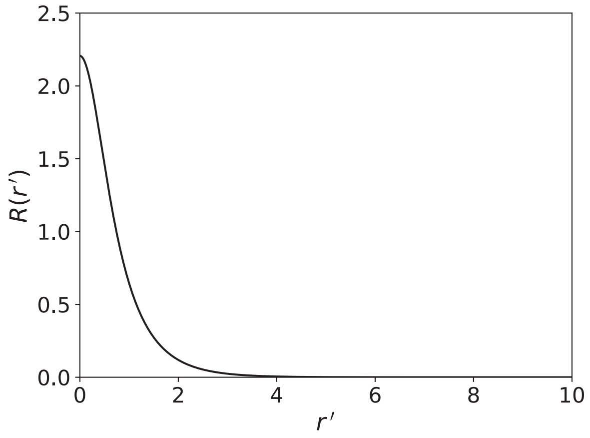

FIG. 5. Numerical solution for the Townes soliton profile $R(r')$ using the shooting method.

A. Review of the Kerr nonlinearity and the dynamics of the Townes soliton ($\chi^{(3)}$ regime)

We start with the analysis of the cubic NLSE, which can be obtained from Eq. (8) for $\gamma|\psi|^2 \ll 1$ in zeroth order, yielding

$$i\frac{\partial\psi}{\partial z'} = -\frac{1}{2}\nabla_\perp'^2\psi - |\psi|^2\psi. \tag{19}$$

If we assume waveguide solutions of the form $\psi = R(r')\exp(iz')$, the stationary equation of motion reduces to

$$\tfrac{1}{2}\nabla'^2 R - R + R^3 = 0, \quad R'(0) = 0, \quad R(\infty) = 0. \tag{20}$$

The solution $R(r')$ above a critical power is a monotonically decreasing function, the Townes soliton [29,47].

Before delving into the physics of the Townes soliton, we review some important aspects of the cubic NLSE. In the context of cold atoms, solitons were investigated in several experiments [48–50]. We note that the dimensionality of the system plays a crucial role. To illustrate this, let us consider a wave packet of size l whose energy functional is given by Eq. (15a). In D spatial dimensions, the cubic NLSE leads to a kinetic term that scales as $E_{\text{kin}} \propto l^{-2}$, while the interaction term goes as $E_{\text{int}} \propto l^{-D}$. For $D = 1$ we know that the energy displays a stable minimum and then bright solitons exist for any interaction strength and atom numbers [49,50]. However, for $D = 3$, the system is dynamic unstable and no solitons can be conceived for this specific case of a Kerr nonlinearity [48,51]. Finally, for $D = 2$, the system does not possess a characteristic length scale. A stationary solution is available only for a discrete value of the interaction strength that makes E_{kin} and E_{int} perfectly balance each other. In our optical system, this value is converted into the critical value of the dimensionless power. This stationary solution is exactly the one obtained by Townes, whose energy is zero and chemical potential is negative. Solving Eq. (20) numerically for an input Gaussian beam using the shooting method, we obtain the Townes soliton shown in Fig. 5.

From the numerical solution of Eq. (20), we compute the dimensionless critical power $\mathcal{P}_{\text{cr}}$ and obtain the value

$$\mathcal{P}_{\text{cr}} = \int |R|^2 d^2\mathbf{r}' = 5.8504. \tag{21}$$

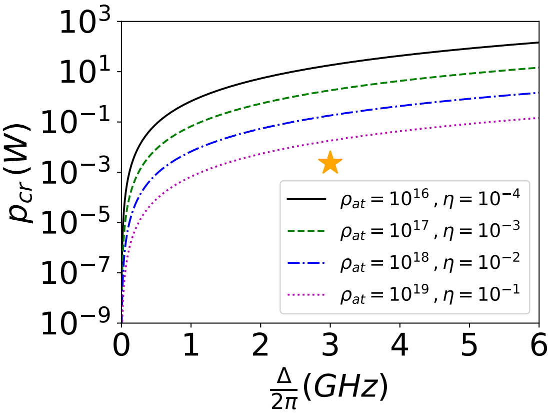

FIG. 6. Matching the Townes soliton condition. The critical power is plotted as a function of the frequency detuning Δ. Each curve is obtained for different values of the dimensionless parameter η, and consequently of the atom density, as identified in the legend. The orange star is computed at $\Delta = 2\pi \times 3.0$ GHz and $\rho_{\text{at}} = 8.3 \times 10^{19}$ m^{-3} (see the main text).

The solutions of Eq. (19) do not blow up provided the dimensionless incident power, i.e., $\mathcal{P} = \int |\psi(r', 0)|^2 d^2\mathbf{r}'$, is strictly below $\mathcal{P}_{\text{cr}}$ [52].

With our simplified two-level description, we can estimate experimental accessible parameters for realizing a Townes soliton in a hot vapor setup. Restoring the units and using the relation between the Rabi frequency and the intensity, we derive an expression for the dimensional critical power which matches the condition given in Eq. (21). In doing so, we obtain

$$p_{\text{cr}} = 8I_{\text{sat}}\left(\frac{5.8504}{k_0^2\eta}\right)\left\{\frac{\Delta/\Gamma}{\left[\left(\frac{\Delta}{\Gamma}\right)^2 + \frac{1}{4}\right]^2}\right\}^{-1}, \tag{22}$$

where I_{sat} is the saturation intensity. In Fig. 6 we show a plot of p_{cr} as a function of Δ for different values of the prefactor η [see Eq. (10)], which in turn depends on the vapor density. As an example, let us consider $\Delta = 2\pi \times 3.0$ GHz and $\rho_{\text{at}} = 8.3 \times 10^{19}$ m^{-3}. For this case, a power close to 2.3 mW would be needed to match the Townes condition given in Eq. (21). This configuration is represented by the orange star in the plot. We compute the value of the nonlinear refractive index n_2 for the same frequency detuning, saturation intensity, and atom density and obtain $n_2 = 1.2 \times 10^{-10}$ m^2/W, in good agreement with the experimental result obtained in [53]. In general, we observe that p_{cr} grows as the value of the prefactor η decreases. In other words, the critical experimental power has higher values as the atom density of the system decreases.

An additional interesting feature of the cubic NLSE is that, for self-focusing beams, the dynamic evolution naturally makes the initial configuration evolve towards the Townes profile regardless of the initial shape of the beam [47]. A neat example is the case of an elliptically shaped input beam, verified experimentally in [54]. We consider the elliptical input beam

$$\psi(x, y) = \sqrt{\frac{\mathcal{P}}{2\pi}}\exp\left(-\frac{x^2}{8} - \frac{y^2}{2}\right), \tag{23}$$

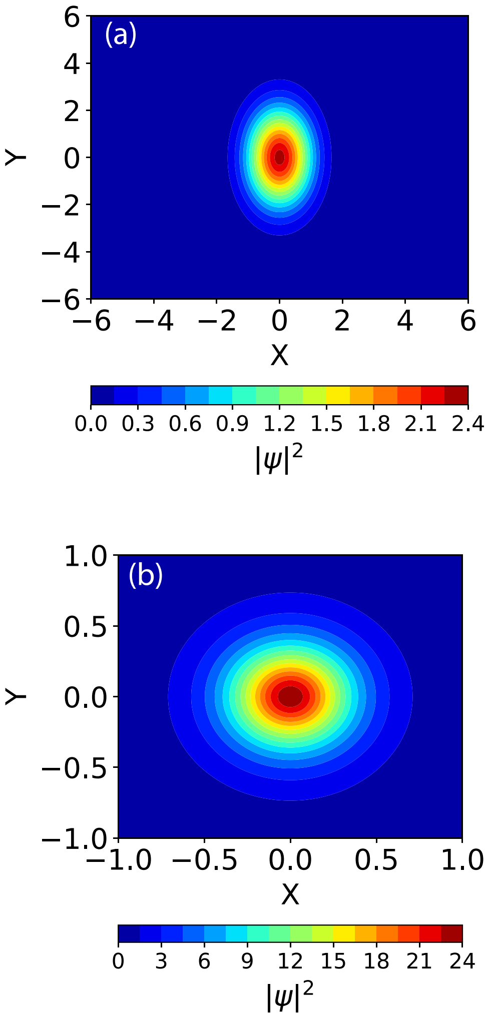

FIG. 7. The $\chi^{(3)}$ regime. (a) Propagation of an elliptically shaped input beam ($z' = 0$) as it evolves with the effective interaction time. (b) As the beam propagates, it self-focuses and a circularly symmetric Townes profile is formed at an intermediate state ($z' = 2.5$) as the beam collapses. To guarantee better visibility of the Townes profile, (b) shows a close-up view.

with scaled power $\mathcal{P} = 14.5$, well above the critical value for beams with this shape. The plots of the intensity profile (I) in Figs. 7(a) and 7(b) display the initial and the intermediate state at $z' = 2.5$ of the real-time evolution, respectively. In this case, the spatial profile of the collapsing elliptical input beam evolves to the circularly symmetric shape profile which characterizes the Townes soliton. Recently, the self-similar evolution related to the Townes soliton physics was investigated in BECs with two components [55] and through the use of a Feshbach resonance [56]. Another remarkable property of the Townes soliton is the scale invariance, recently verified in a 2D Bose gas [57]. From a given stationary solution $R(r')$, we can build a family of solutions with the same critical power through a dilation operation [44]. Higher nonlinearities explicitly break scale invariance. Nevertheless, in the limit where the stationary solution is characterized by a power slightly above the critical value, the higher-order nonlinearities can be neglected and the solutions resemble the Townes soliton profile for a long propagation length.

Finally, we investigate aspects related to the collapsing behavior of this solution: an exact Townes shape remains stable in time evolution, but perturbations in shape will lead to unstable solutions. Following the approach in [58], we derive an expression for the critical distance for the collapsing of the wave packet.

Consider the ansatz for the wave function $\psi(\mathbf{r}, z)$,

$$\psi(\mathbf{r}, z) = A(z) M\left(\frac{r}{a(z)}\right) \exp[i\theta(r, z)], \tag{24}$$

where $A(z)$ is a complex-valued amplitude, $a(z)$ is the wave radius, and $M(r/a(z))$ is a real function describing the profile. The general expression for $a(z)$ can be found by following a variational procedure which involves obtaining the Lagrangian and later the equations of motion of the system and solving them for the variable $a(z)$. Following this procedure, we obtain the expression

$$a(z) = a_0\left[(z\sqrt{2\mu})^2\left(1 - \frac{\nu}{\mu}\right) + 1\right]^{1/2}, \tag{25}$$

where $a_0 \equiv a(0) \neq 0$ is the initial wave radius and $\dot{a}(0) = 0$. The parameters μ and ν are given in terms of the initial conditions and integrals of the profile $M(r/a(z))$. (See Appendix B for a detailed derivation.)

From Eq. (25) we determine the collapse distance by setting $a(z_{\text{cr}}) = 0$, which yields

$$z_{\text{cr}} = \frac{1}{\sqrt{2(\nu - \mu)}}. \tag{26}$$

We provide explicit results for two different test functions, a Gaussian form (GS) and the hyperbolic secant (HS),

$$M\left(\frac{r}{a(z)}\right) = \begin{cases} \exp\left(-\frac{r^2}{2a^2}\right) & \text{(GS)} \\ \sqrt{2}\operatorname{sech}\left(\frac{r}{a}\right) & \text{(HS)}. \end{cases} \tag{27}$$

For each of these test functions, we compute the integrals for the coefficients μ and ν, leading to the following expressions for $a(z)$:

$$a(z) = \begin{cases} a_0\sqrt{\frac{z^2}{a_0^8}\left(1 - \frac{\mathcal{P}a_0^2}{2\pi}\right) + 1} & \text{(GS)} \\ \frac{a_0}{3}\sqrt{\frac{2z^2}{\zeta(3)a_0^8}\left[\frac{2(1+\ln 4)}{3} - \frac{\mathcal{P}(1+\ln 16)a_0^2}{\pi \ln 2}\right] + 1} & \text{(HS)}. \end{cases} \tag{28}$$

In Fig. 8 we show the critical distance z_{cr} as a function of the frequency detuning. The values considered for the incident power are equal to $p = 0.4$ and 1.5 W, while the initial wave radius a_0 is chosen to be equal to the beam waist $w_0 = 7 \times 10^{-4}$ m. The results show that the collapse distance z_{cr} decreases upon increasing the incident power. Also, we observe that the detuning range is consistent with the allowed ranges of Fig. 3.

B. Dynamics of the breathing mode

In this section we analyze the breathing mode in the droplet dynamics. In the context of ultracold Bose-Bose mixtures, there have been recent studies aiming at understanding the

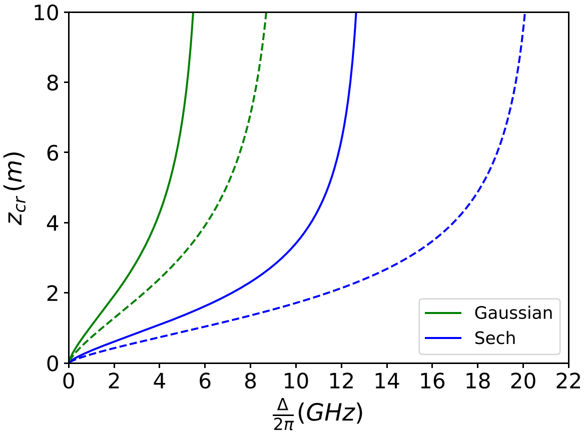

FIG. 8. Collapse analysis. Critical distance z_{cr} as a function of the frequency detuning Δ considering different profiles for the test function $M(r/a(z))$. The solid curves correspond to the incident power $p = 0.4$ W and the dashed ones to $p = 1.5$ W.

relevant processes involved in the formation of metastable droplets from out-of-equilibrium mixtures [59–62]. In certain regimes, droplets cannot sustain any discrete excitation since all the excited energy states are higher in energy than the particle emission threshold, hence the name self-evaporation process. Because of that, the droplet is able to dissipate any excess energy by releasing atoms or breaking up into smaller pieces.

For the optical system considered in this work, we derive the analytical expressions for the chemical potential for both the $\chi^{(3)} + \chi^{(5)}$ and saturating regimes. Considering the Gaussian variational ansatz introduced in Sec. III, the breathing frequency ω is obtained by expanding the energy in the vicinity of $\sigma' = \sigma_c'$.

For the $\chi^{(3)} + \chi^{(5)}$ regime, we can show that

$$\omega = \sqrt{-\frac{81\pi(2\pi - \mathcal{P})^3}{256\mathcal{P}^3\gamma^2}}, \tag{29}$$

with $\mathcal{P} > 2\pi$. The chemical potential is obtained from the time-dependent NLSE given in Eq. (17), which results in

$$\mu^{(5)} = \left(\frac{1}{2}\int |\nabla\psi(\mathbf{r}', z')|^2 d^2\mathbf{r}' - \int |\psi(\mathbf{r}', z')|^4 d^2\mathbf{r}' + 2\gamma\int |\psi(\mathbf{r}', z')|^6 d^2\mathbf{r}'\right)\Big/\int |\psi(\mathbf{r}', z')|^2 d^2\mathbf{r}'.$$

In the Gaussian approximation of Eq. (13) we obtain

$$\mu^{(5)} = \frac{1}{2\sigma'^2} - \frac{\mathcal{P}}{2\pi\sigma'^2} + \frac{2\gamma\mathcal{P}^2}{3\pi^2\sigma'^4} \tag{30}$$

for the general expression of the chemical potential. A further evaluation of this expression at $\sigma' = \sigma_c'$ yields

$$\mu^{(5)}(\mathcal{P}, \gamma, \sigma' = \sigma_c') = \frac{9(4\pi^2 - \mathcal{P}^2)}{128\gamma\mathcal{P}^2}. \tag{31}$$

For the saturating regime, an analytical expression for ω is not available. On the other hand, the chemical potential is computed from Eq. (8), which gives

$$\mu^{(\mathrm{sat})} = \left(\frac{1}{2}\int |\nabla\psi(\mathbf{r}')|^2 d^2\mathbf{r}' - \int \frac{|\psi(\mathbf{r}')|^4}{1 + 2\gamma|\psi(\mathbf{r}')|^2} d^2\mathbf{r}'\right)\Big/\int |\psi(\mathbf{r}')|^2 d^2\mathbf{r}'.$$

Within the Gaussian approximation the expression above reads

$$\mu^{(\mathrm{sat})} = \frac{1}{2\sigma'^2} - \frac{1}{2\gamma} + \frac{\pi\sigma'^2}{4\gamma^2\mathcal{P}}\ln\left(1 + \frac{2\gamma}{\pi\sigma'^2}\mathcal{P}\right). \tag{32}$$

With these expressions, we define the range of parameters to observe the breathing mode or the self-evaporation.

To identify the behaviors of interest, we look at the cases in which $\omega/|\mu| \geqslant 1$ and $\omega/|\mu| < 1$. The former indicates the region where no monopole excitation can be observed, while the latter is the case where monopole excitations are present. In the numerical simulations, the breathing mode is excited by changing the intensity, i.e., $|\psi|^2$, of the ground state by a factor of 1.05. In the context of a BEC, this would be equivalent to a slight increase of the particle number. Subsequently, the frequency ω is obtained numerically through the Fourier analysis of the droplet width $\sigma_{r'}(z)$. In order to avoid spurious reflections of the wave function that may take place at the boundary of the computational domain, we use absorbing boundary conditions.

In Fig. 9(a) we display the ratio of the breathing frequency and the chemical potential for different regimes, following the predictions from the Gaussian ansatz and the results obtained from numerical simulations at an incident power $p = 0.4$ W. The system does not support a breathing mode, as the excitation energy is greater than the chemical potential for a wide range of allowed values of Δ. There the droplet width does not undergo sinusoidal oscillations [see Figs. 10(a) and 10(b) for the $\chi^{(3)} + \chi^{(5)}$ and saturating regimes, respectively]: $\sigma_r(z)$ has an initial increase and then decays approaching the value of equilibrium, that is, the droplet width for the ground state. This is the behavior for the entire window of Δ in which $\omega/|\mu| \geqslant 1$.

However, there will still be a very limited region which is characterized by the values of Δ whose curves are below the horizontal green dashed line which represents the case that $\omega = |\mu|$ and this can be seen in more detail in the inset in Fig. 9(a). In this very narrow region, $\sigma_r(z)$ shows sinusoidal oscillations, as can be seen in Figs. 10(c) and 10(d).

Before proceeding, we provide a broader analysis of the existence of the breathing mode for the $\chi^{(3)} + \chi^{(5)}$ regime. With the aid of Eqs. (29) and (31), we compute the ratio $\omega/|\mu|$. For this calculation, we should take into account the fact that, when $\Delta > 0$, γ is always positive [see its definition in Eq. (9b)], in addition to obeying the constraint over the values of $\mathcal{P}$ that they should be greater than 2π. In doing so, we arrive at the following expression:

$$\frac{\omega}{|\mu|} = \frac{8\sqrt{(\mathcal{P} - 2\pi)\pi\mathcal{P}}}{\mathcal{P} + 2\pi}. \tag{33}$$

Thus, we see that the resulting expression is independent of γ for the $\chi^{(3)} + \chi^{(5)}$ regime. It is easy to check that this expression is smaller than unity for values of $\mathcal{P}/\mathcal{P}_{\mathrm{cr}}$ contained in the

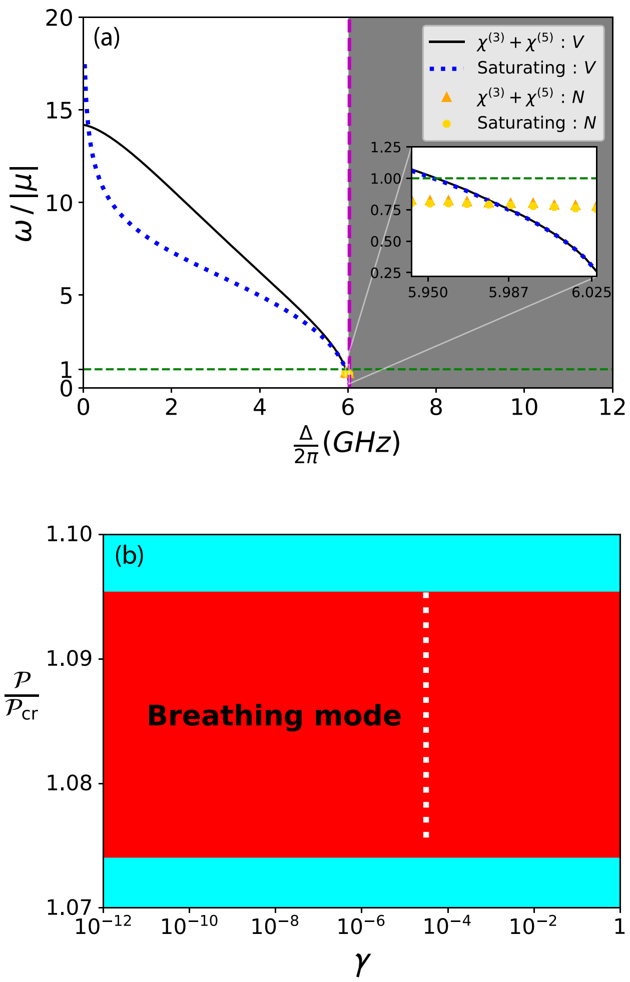

FIG. 9. (a) Ratio between the excitation energy ω and the absolute value of the chemical potential $|\mu|$. The value of the incident power is $p = 0.4$ W. The curves with markers refer to the numerical results (N): orange triangles for the $\chi^{(3)} + \chi^{(5)}$ regime and yellow octagons for the saturating regime. For variational results (V), the black solid line is for the $\chi^{(3)} + \chi^{(5)}$ case and the blue dotted line is for the saturating case. The inset shows the narrow region where $\omega/|\mu| < 1$, which represents the sector where the breathing mode can be found. (b) Dynamical phase diagram for the breathing mode (red region) obtained via the Gaussian variational ansatz for the $\chi^{(3)} + \chi^{(5)}$ regime according to Eq. (33). The white dotted line corresponds to the points shown in (a) for $\omega/|\mu|$ as a function of Δ belonging to the breathing region for the same regime.

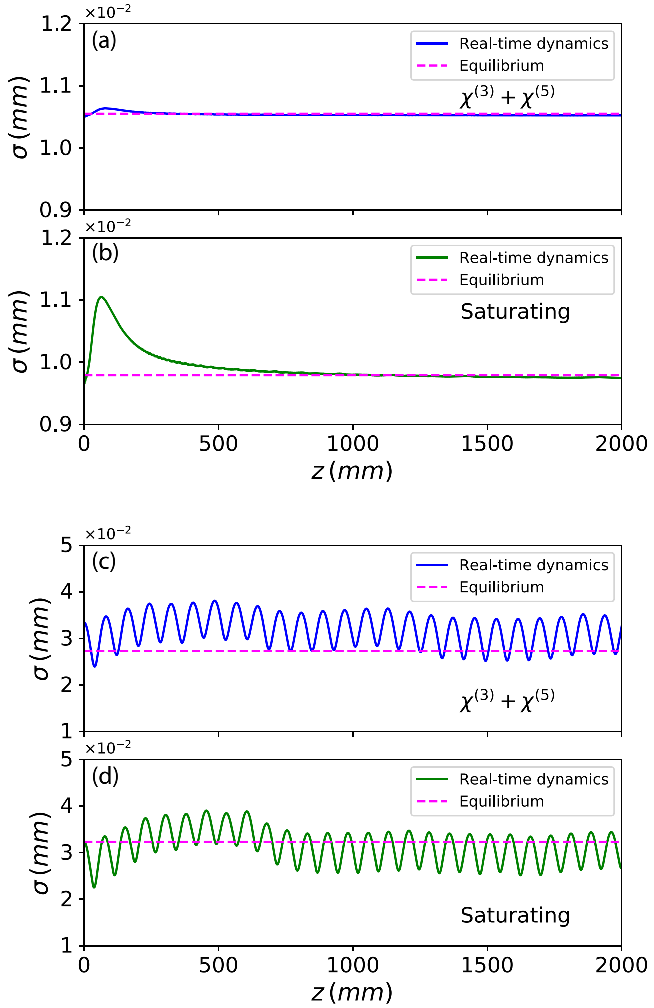

FIG. 10. Evolution of the droplet width $\sigma_r(z)$ for the two-level system for both the (a) and (c) $\chi^{(3)} + \chi^{(5)}$ (blue solid curves) and (b) and (d) saturating (green solid curves) regimes for (a) and (b) $\Delta = 2\pi \times 3.0$ GHz and (c) and (d) $\Delta = 2\pi \times 6.0$ GHz. The horizontal magenta dashed lines show the stationary equilibrium values. The power is chosen to be $p = 0.4\ W$.

interval (1.074,1.095). The phase diagram for this situation is represented by the red region in Fig. 9(b). In the same plot, the parametric (white dotted) curve corresponds to the configuration presented in Fig. 9(a) in the narrow window of the values of Δ for which the breathing mode can be excited. In other words, it represents the mapping of the points mentioned above onto the $\mathcal{P}/\mathcal{P}_{\rm cr}$-$\gamma$ plane.

For the specific case analyzed above and shown in Fig. 9(a), the configuration representing the nonoscillatory region is displayed in Figs. 10(a) and 10(b) and corresponds to $\mathcal{P}/\mathcal{P}_{\rm cr} \sim 3.02$, while for the one belonging to the oscillatory region, which is represented in Figs. 10(c) and 10(d), we have $\mathcal{P}/\mathcal{P}_{\rm cr} \sim 1.075$, slightly above the lower bound set by the Gaussian variational ansatz. Therefore, such values corroborate the predictions obtained through the variational analysis for the $\chi^{(3)} + \chi^{(5)}$ regime.

Next we turn our attention to the self-evaporation mechanism by looking at the fraction of power that is lost so that the system can then relax to its equilibrium state. Figure 11 shows the numerical results for the ratio between the final ($\mathcal{P}_f$) and the initial power ($\mathcal{P}_i$), revealing that a tiny fraction of power is lost through self-evaporation in this regime.

C. Dynamics for a Gaussian input beam under realistic experimental conditions

We now analyze the dynamics for the realistic experimental case for a Gaussian input beam. We show the results obtained from 2D numerical simulations of Eqs. (8) and (17) for the intensity profiles of the system by setting $p = 0.4$ W and the

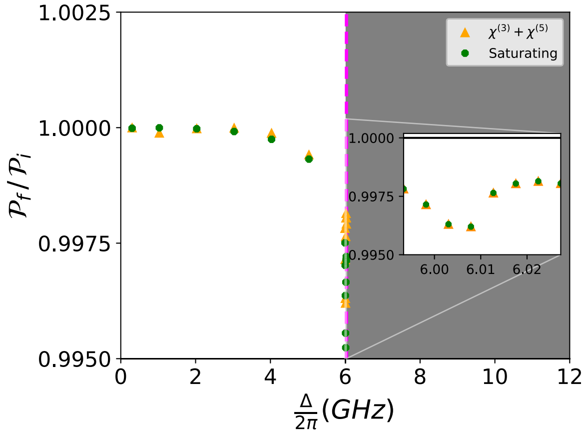

FIG. 11. Fraction of power lost due to the self-evaporation mechanism obtained from the numerical simulations of the NLSE. Orange triangles represent the $\chi^{(3)}+\chi^{(5)}$ regime and green octagons refer to the saturating case. The value of the incident power is $p = 0.4$ W. The inset shows a close-up of the region where more points were analyzed, which the Gaussian variational approach predicts to be within the region in which the breathing mode can exist.

initial beam waist equal to 0.1 mm. We let the system evolve for a distance $z_R \approx 2.0$ m.

In the density plots of Figs. 12(a) and 13(a), for $\Delta = 2\pi \times 6.0$ GHz, we show the initial state of the system for the $\chi^{(3)}+\chi^{(5)}$ and saturating regimes, respectively. As the beam travels through the nonlinear medium, we observe that the system oscillates with decreasing amplitude as the time evolves. This oscillatory behavior around the equilibrium configuration of the system is depicted in Figs. 12(b) and 13(b), which show a cut along $y = 0$. The equilibrium states are obtained through imaginary-time simulations of Eqs. (8) and (17). Due to the use of absorbing boundary conditions, the curves obtained through propagation in real time shown in these plots do not overlap perfectly the ones of the equilibrium states. Before moving on, we briefly describe two examples of previous experiments with cold atoms [63] and hot vapors [13]. We verify whether the range of experimental parameters used in them were optimal for observing droplets of light. For the former, it was shown that, for a near-resonant propagating beam, a large cloud of cold ^{87}Rb atoms acts as a saturable Kerr medium and produces self-trapping of light, that is, the waist remains stationary for an appropriate choice of parameters. For that experiment, the value of the ratio $\mathcal{P}/\mathcal{P}_{\rm cr}$ is approximately 1.9 and $\gamma = 0.20$, which is a highly saturated regime. Much of the cloud is contained in the droplet region based on our phase diagram in Fig. 4. Nevertheless, if we compute the ratio $\omega/|\mu|$, it is greater than unity, so we will not be able to see the manifestation of the breathing mode. For the latter, the out-of-equilibrium dynamics of a two-dimensional paraxial fluid of light is analyzed using a near-resonant laser propagating through a hot atomic vapor and the formation of shock waves. For this experiment, $\mathcal{P}/\mathcal{P}_{\rm cr} > 1$ for a broad range of the frequency detuning and we can eventually reach conditions by increasing Δ for which the observation of the breathing mode is possible, although at this point it is uncertain whether this would occur for realistic propagation lengths, and consequently a more careful analysis supported by numerical simulations would be required.

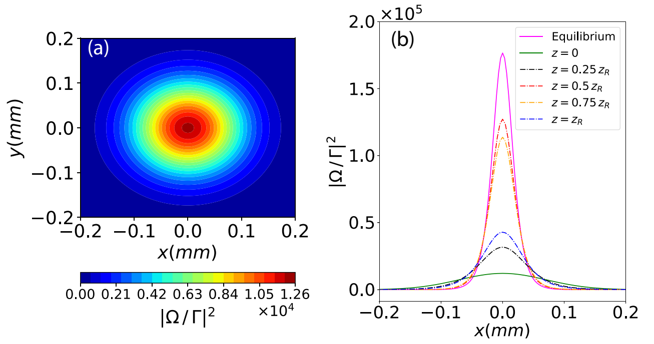

FIG. 13. (a) Density plot showing the input beam for the saturating regime when $\Delta = 2\pi \times 6.0$ GHz. (b) Cut along the y axis, $|\Omega(z, x, 0)/\Gamma|^2$, displaying the evolution of the input beam at different effective lengths.

Figures 14 and 15 display the results for $\Delta = 2\pi \times 3.0$ GHz for the $\chi^{(3)}+\chi^{(5)}$ and saturating regimes, respectively. Again, the oscillatory behavior around the equilibrium is present. Nevertheless, it is clear that the shrinkage of the

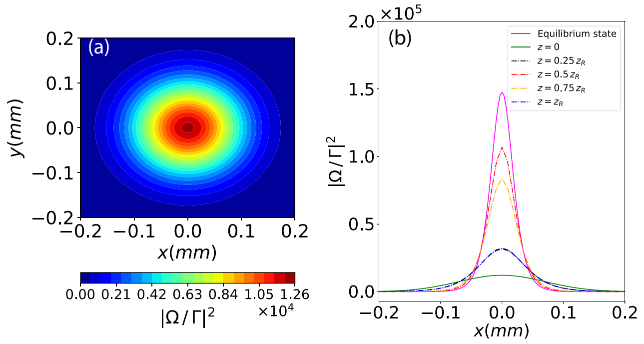

FIG. 12. (a) Density plot showing the input beam for the $\chi^{(3)}+\chi^{(5)}$ regime when $\Delta = 2\pi \times 6.0$ GHz. (b) Cut along the y axis, $|\Omega(z, x, 0)/\Gamma|^2$, displaying the evolution of the input beam at different effective lengths.

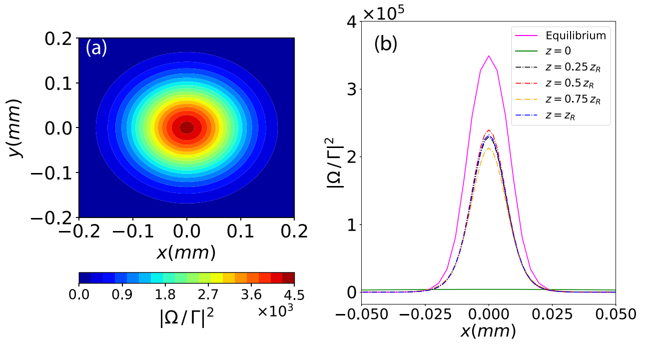

FIG. 14. 2D numerical simulations. (a) Density plot showing the input beam for the $\chi^{(3)}+\chi^{(5)}$ regime when $\Delta = 2\pi \times 3.0$ GHz. (b) Cut along the y axis, $|\Omega(z, x, 0)/\Gamma|^2$, displaying the evolution of the input beam at different effective lengths.

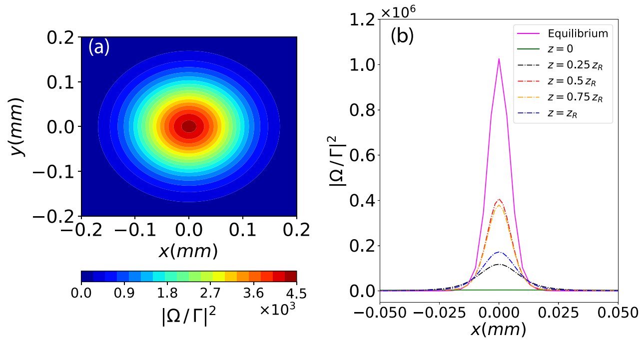

FIG. 15. 2D numerical simulations. (a) Density plot showing the input beam for the saturating regime when $\Delta = 2\pi \times 3.0\,\text{GHz}$. (b) Cut along the y axis, $|\Omega(z, x, 0)/\Gamma|^2$, displaying the evolution of the input beam at different effective lengths.

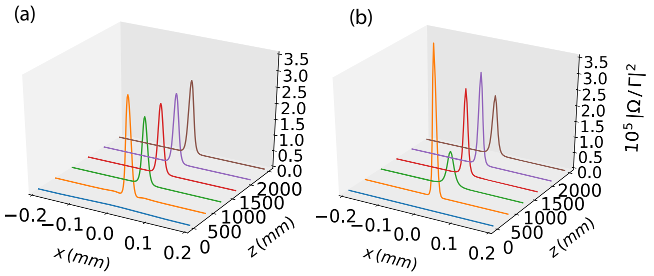

FIG. 17. 2D numerical simulations. Cut along the transversal y direction of the intensity profile for (a) the $\chi^{(3)} + \chi^{(5)}$ regime and (b) the saturating regime for $\Delta = 2\pi \times 3.0$ GHz.

input beam is much more pronounced than that observed for $\Delta = 2\pi \times 6.0$ GHz and this only gets more accentuated as the frequency detuning is decreased (strength of the nonlinearity increases).

Actually, this strong effect of the nonlinearity that makes the input beam shrink to a point leads to difficulties in the numerical simulations, as problems with spatial resolution start to appear. Furthermore, as we approach the resonance, the radial symmetry starts to break down and because of that, 1D and 2D numerical simulations display very opposite behavior for this system in this region. In fact, 1D simulations are not adequate to represent the dynamics of the system close to resonance. A faithful representation of the dynamics of the system in this region is only possible and reliable through full 2D numerical simulations. To give an estimate of at what point the 1D and 2D numerical simulations stop agreeing, we compare the curves obtained for the intensity and find that there is a quite fair overlap until $\Delta = 2\pi \times 3.0$ GHz.

This inconsistency can be made more clear if we check the outcomes of numerical simulations for lower values of Δ. For the full 2D case, different dynamical behaviors can emerge. One of them is that the input beam, due to the strong nonlinearity, can eventually shrink dramatically such that it breaks completely into small fragments, even for short propagation effective lengths. This fragmentation process in the optical system considered here could be linked to the results of the physics investigated in [56], in which the universal nonequilibrium dynamics in degenerate 2D Bose gases was investigated. The authors considered an initially large sample and then performed a quench from repulsive (defocusing) to attractive (focusing) interactions through the use of a Feshbach resonance. If the appropriate regime is reached, which means that the value of the product between particle number and interacting strength $N|g|$ is close to the Townes threshold, then this quench procedure makes possible the observation of the dynamic formation of Townes solitons from modulational instability (MI). The MI breaks up the initial sample into fragments, universally around the Townes threshold. We leave the detailed investigation of fragmentation within our model for future work.

Finally, we compare the dynamics for the different regimes in this realistic scenario. In Figs. 16 and 17 we show the integrated beam profile for the $\chi^{(3)} + \chi^{(5)}$ and saturating regimes for $\Delta = 2\pi \times 6.0$ and $2\pi \times 3.0$ GHz, while in Fig. 18 we display the results for the $\chi^{(3)}$ regime. It is clear how the effect of self-focusing makes the width of the intensity profile in the $\chi^{(3)}$ regime shrink dramatically when compared to the other two regimes, in which the defocusing effect of $\chi^{(5)}$ and the saturation hinder this focusing behavior.

V. CONCLUSION

Motivated by recent experiments on quantum fluids of light well described within the paraxial approximation and their analogy to Bose-Einstein condensates described by the Gross-Pitaevskii equation, we investigated the conditions to observe droplets of light in nonlinear optical media. We reviewed the cubic focusing NLSE and the physics of the Townes soliton. For this regime, it is known that self-bound states cannot

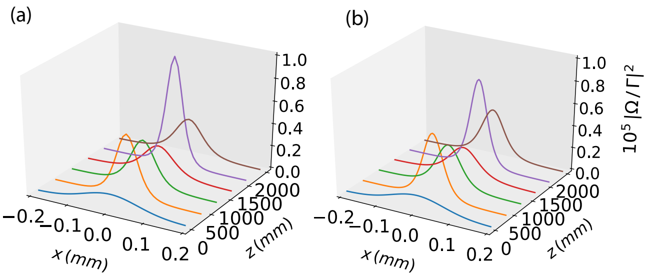

FIG. 16. 2D numerical simulations. Cut along the transversal y direction of the intensity profile for (a) the $\chi^{(3)} + \chi^{(5)}$ regime and (b) the saturating regime for $\Delta = 2\pi \times 6.0$ GHz.

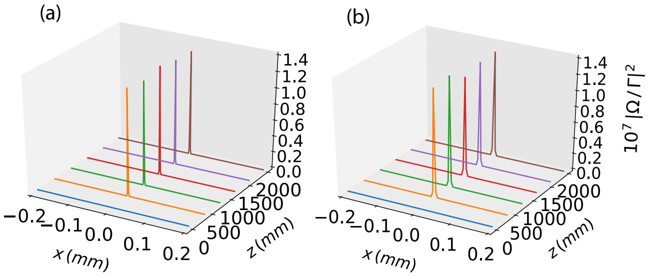

FIG. 18. 2D numerical simulations. Cut along the transversal y direction of the intensity profile for the $\chi^{(3)}$ regime considering (a) $\Delta = 2\pi \times 3.0$ GHz and (b) $\Delta = 2\pi \times 6.0$ GHz.

be formed as there is no mechanism to compensate for the combined repulsive effects due to diffraction and the focusing (attractive) Kerr nonlinearity. When anomalous second-order dispersion is taken into account, the system becomes $3+1$ dimensional with the proper time playing the role of a third spatial coordinate. In this scenario, the existence of optical bullets was foreseen [64], though these structures would be unstable. We then concentrated our efforts on the $\chi^{(3)}+\chi^{(5)}$ and saturating nonlinearities. For the cubic-quintic NLSE, several works had already pointed out the possibility of having self-bound states [36], while for the saturating regime only the optical bullets were predicted in the presence of anomalous dispersion [65]. By using the variational Gaussian ansatz approach, we obtained an analytical expression for the radial width of the droplet of light for the $\chi^{(3)}+\chi^{(5)}$ regime. The variational results were then compared with numerical simulations. We found good agreement, certifying the reliability of the variational method. We also investigated the dynamics of the breathing mode and how the self-evaporation mechanism can influence the dynamical process of formation of droplets of light for both the $\chi^{(3)}+\chi^{(5)}$ and saturating regimes. Our study revealed that the system may sustain collective excitations only for a very limited region of the frequency detuning, while overdamped oscillations are present in a wide range of Δ. This analysis can be made broader when translated in terms of the parameters $\mathcal{P}/\mathcal{P}_{\text{cr}}$ and γ. We made it for the $\chi^{(3)}+\chi^{(5)}$ regime for which the ratio $\omega/|\mu|$ has an analytical expression. For the saturating regime, an extensive numerical analysis is required. We found that the breathing mode can be excited in a very narrow range of the values of $\mathcal{P}/\mathcal{P}_{\text{cr}}$ and that it is independent of the parameter γ. For realistic experimental conditions, we employed 1D and 2D numerical simulations. The former predicted that close to resonance a flat-top profile is formed for the $\chi^{(3)}+\chi^{(5)}$ regime and an oscillatory behavior in the saturating case. However, refined 2D numerical simulations revealed that, close to resonance, the radial symmetry no longer holds, with the input beam becoming susceptible to fragmentation for the regimes of interest. On the other hand, if we consider increasing frequency detuning, the behavior shown by the system becomes very similar for both regimes with identical 1D or 2D simulation results. In conclusion, this study enabled us to establish the values of experimental parameters for which the droplet states can be observed in platforms such as hot atomic vapors and to predict some important aspects of the formation of such self-bound light states. Extensions of this work may include a detailed study of the stability of these droplets and a refinement of our model by extending it for lower values of the frequency detuning with the addition of thermal effects brought about by the Doppler broadening, collisional effects, and the inclusion of absorption. For the thermal effects, there have been recent studies using ultrafast laser fields in which such obstacles can be overcome [66,67]. Nevertheless, in the case of a hot vapor, thermal effects may significantly alter the dynamics of the system close to resonance. On the other hand, we can also advance the understanding of the self-evaporation mechanism and the effects of effective nonlocal nonlinearities [68]. The presence of nonlocality might determine the formation of nontrivial patterns, similar to the case of ultracold Bose gases with magnetic [69,70] or soft-core interactions [71–74]. Finally, a better understanding of multilevel atomic configurations [75] as well as the realization of optical droplets in such cases is another possible and exciting path to be pursued [76].

ACKNOWLEDGMENTS

We thank J. Dalibard for pointing out a related work in the context of 2D Bose mixtures [77]. We gratefully acknowledge insightful discussions with P. Azam, A. Marini, F. Maucher, T. Pohl, H. F. Silva, V. Zampronio, and B. Bakkali-Hassani and J. Beugnon for a critical reading of the manuscript. This study was financed in part by the Coordenação de Aperfeiçoamento de Pessoal de Nível Superior–Brasil (CAPES)–Finance Code 001. T.M. acknowledges the hospitality of the Institut de Physique de Nice, Valbonne, where this work was initiated. This work was supported by the Serrapilheira Institute (Grant No. Serra-1812-27802) and CAPES-NUFFIC Project No. 88887.156521/2017-00. This research was developed with the help of the XMDS2 software package [78]. We thank the High Performance Computing Center (NPAD) at UFRN for providing computational resources.

APPENDIX A: OPTICAL BLOCH EQUATIONS FOR THE TWO-LEVEL SYSTEM

This Appendix is devoted to the presentation of the optical Bloch equations for the two-level system considered in this work and their corresponding solutions for the coherences and populations in the steady state. The characterization of this system was given in Sec. II. The OBEs for the two-level configuration after having applied the rotating-wave approximation are given by

$$\dot{\rho}_{gg} = i\frac{\Omega}{2}\rho_{ge} - i\frac{\Omega^*}{2}\rho_{eg} + \Gamma\rho_{ee}, \tag{A1a}$$

$$\dot{\rho}_{ee} = -i\frac{\Omega}{2}\rho_{ge} + i\frac{\Omega^*}{2}\rho_{eg} - \Gamma\rho_{ee}, \tag{A1b}$$

$$\dot{\rho}_{ge} = -i\Delta\rho_{ge} - i\frac{\Omega^*}{2}(\rho_{ee} - \rho_{gg}) - \frac{\Gamma}{2}\rho_{ge}, \tag{A1c}$$

$$\dot{\rho}_{eg} = i\Delta\rho_{eg} + i\frac{\Omega}{2}(\rho_{ee} - \rho_{gg}) - \frac{\Gamma}{2}\rho_{eg}, \tag{A1d}$$

where $\Delta \equiv \omega - (\omega_e - \omega_g)$ is the frequency detuning. If we solve for the steady state, then the expressions for the populations and coherences are simply

$$\rho_{gg} = \frac{\Gamma^2 + 4\Delta^2 + |\Omega|^2}{\Gamma^2 + 4\Delta^2 + 2|\Omega|^2}, \tag{A2a}$$

$$\rho_{ee} = \frac{|\Omega|^2}{\Gamma^2 + 4\Delta^2 + 2|\Omega|^2}, \tag{A2b}$$

$$\rho_{ge} = \frac{(i\Gamma + 2\Delta)\Omega^*}{\Gamma^2 + 4\Delta^2 + 2|\Omega|^2}, \tag{A2c}$$

$$\rho_{eg} = \frac{(-i\Gamma + 2\Delta)\Omega}{\Gamma^2 + 4\Delta^2 + 2|\Omega|^2}. \tag{A2d}$$

APPENDIX B: WAVE COLLAPSE IN THE $\chi^{(3)}$ REGIME: A VARIATIONAL APPROACH

In this Appendix we derive the expression of the collapsing distance z_{cr} for the cubic NLSE. This derivation follows a similar analysis introduced in [58].

The Lagrangian density for the cubic NLSE given in Eq. (19) is

$$\mathcal{L} = \frac{i}{2}(\psi^*\partial_z\psi - \psi\partial_z\psi^*) - \mathcal{H}, \quad \mathcal{H} = \left|\frac{\partial\psi}{\partial r}\right|^2 - \frac{|\psi|^4}{2}. \tag{B1}$$

Next we build an ansatz for the wave function $\psi(r, z)$. We assume a self-similar trial function

$$\psi(\mathbf{r}, z) = A(z)M\left(\frac{r}{a(z)}\right)\exp[i\theta(r, z)], \tag{B2}$$

where $M(r/a(z))$ is an arbitrary real profile function only depending on the spatial coordinate $\xi = r/a(z)$ rescaled with respect to the wave radius $a(z)$ and $A(z)$ is a normalization factor at distance z. Plugging this ansatz into Eq. (B1) and integrating over the radial coordinates yields

$$L = -|A|^2a^2\left\{\alpha_0\dot{\theta}_0 + \alpha_2 a^2\left[\dot{\theta}_2 + 2\theta_2^2\right] + \frac{\lambda}{2a^2} - \frac{|A|^2\beta}{2}\right\}. \tag{B3}$$

The coefficients

$$\alpha_m \equiv \|r^{m/2}M\|_2, \quad \beta \equiv \|M\|_4, \quad \lambda \equiv \|\partial_r M\|_2, \tag{B4}$$

where we define $\|f\|_p = 2\pi\int_0^{+\infty} f^p(r) r\,dr$. Let us now consider $A(z)$, $\theta_0(z)$, $\theta_2(z)$, and $a(z)$ as canonical variables. We are then led to the dynamical equations

$$\begin{aligned} |A|^2a^2 &= P = \text{const}, \\ \theta_2(z) &= \frac{\dot{a}}{2a}, \\ \frac{d^2a}{dz^2} &= \frac{\lambda}{\alpha_2 a^3} - \frac{P\beta}{\alpha_2 a^3}, \end{aligned} \tag{B5}$$

and by multiplying both sides of the equation for $a(z)$ by $\dot{a}(z)$, the remaining expression can be easily integrated, which results in

$$\frac{1}{2}\left[\frac{d}{dz}\left(\frac{a}{a_0}\right)\right]^2 + \Pi\left(\frac{a}{a_0}\right) = 0, \tag{B6}$$

with

$$\Pi(x) \equiv (\mu - \nu)\left(\frac{1}{x^2} - 1\right), \quad \mu \equiv \frac{2\lambda}{\alpha_2 a_0^4}, \quad \nu \equiv \frac{|A_0|^2\beta}{\alpha_2 a_0^2}, \tag{B7}$$

which applies to the case in which $a_0 \equiv a(z = 0) \neq 0$ and $\dot{a}(0) = \dot{a}(z = 0) = 0$. It follows that the solution for Eq. (B6) becomes

$$a(z) = a_0\left[(z\sqrt{2\mu})^2\left(1 - \frac{\nu}{\mu}\right) + 1\right]^{1/2}, \tag{B8}$$

which predicts that the wave collapses with $a(z) \to 0$ at the finite distance

$$z_{cr} = \frac{1}{\sqrt{2(\nu - \mu)}}, \tag{B9}$$

under the constraint that $\nu/\mu > 1$. In the main text, this expression was applied, considering different forms for the function $M(r/a(z))$ and with a_0 being the beam waist.

---

[1] I. Carusotto and C. Ciuti, Rev. Mod. Phys. **85**, 299 (2013).

[2] Q. Glorieux, T. Aladjidi, P. D. Lett, and R. Kaiser, arXiv:2209.04622.

[3] C. Connaughton, C. Josserand, A. Picozzi, Y. Pomeau, and S. Rica, Phys. Rev. Lett. **95**, 263901 (2005).

[4] N. Šantić, A. Fusaro, S. Salem, J. Garnier, A. Picozzi, and R. Kaiser, Phys. Rev. Lett. **120**, 055301 (2018).

[5] K. Baudin, A. Fusaro, K. Krupa, J. Garnier, S. Rica, G. Millot, and A. Picozzi, Phys. Rev. Lett. **125**, 244101 (2020).

[6] I. Carusotto, Proc. R. Soc. A **470**, 20140320 (2014).

[7] Q. Fontaine, T. Bienaimé, S. Pigeon, E. Giacobino, A. Bramati, and Q. Glorieux, Phys. Rev. Lett. **121**, 183604 (2018).

[8] Q. Fontaine, P.-E. Larré, G. Lerario, T. Bienaimé, S. Pigeon, D. Faccio, I. Carusotto, E. Giacobino, A. Bramati, and Q. Glorieux, Phys. Rev. Res. **2**, 043297 (2020).

[9] P. Azam, A. Griffin, S. Nazarenko, and R. Kaiser, Phys. Rev. A **105**, 043510 (2022).

[10] M. Isoard, A. M. Kamchatnov, and N. Pavloff, Phys. Rev. A **99**, 053819 (2019).

[11] S. K. Ivanov, J.-E. Suchorski, A. M. Kamchatnov, M. Isoard, and N. Pavloff, Phys. Rev. E **102**, 032215 (2020).

[12] S. A. Simmons, F. A. Bayocboc, J. C. Pillay, D. Colas, I. P. McCulloch, and K. V. Kheruntsyan, Phys. Rev. Lett. **125**, 180401 (2020).

[13] P. Azam, A. Fusaro, Q. Fontaine, J. Garnier, A. Bramati, A. Picozzi, R. Kaiser, Q. Glorieux, and T. Bienaimé, Phys. Rev. A **104**, 013515 (2021).

[14] T. Bienaimé, M. Isoard, Q. Fontaine, A. Bramati, A. M. Kamchatnov, Q. Glorieux, and N. Pavloff, Phys. Rev. Lett. **126**, 183901 (2021).

[15] M. Abuzarli, T. Bienaimé, E. Giacobino, A. Bramati, and Q. Glorieux, Europhys. Lett. **134**, 24001 (2021).

[16] G. I. Martone, T. Bienaimé, and N. Cherroret, Phys. Rev. A **104**, 013510 (2021).

[17] J. Steinhauer, M. Abuzarli, T. Aladjidi, T. Bienaimé, C. Piekarski, W. Liu, E. Giacobino, A. Bramati, and Q. Glorieux, Nat. Commun. **13**, 2890 (2022).

[18] D. S. Petrov, Phys. Rev. Lett. **115**, 155302 (2015).

[19] M. Schmitt, M. Wenzel, F. Böttcher, I. Ferrier-Barbut, and T. Pfau, Nature (London) **539**, 259 (2016).

[20] L. Chomaz, S. Baier, D. Petter, M. J. Mark, F. Wächtler, L. Santos, and F. Ferlaino, Phys. Rev. X **6**, 041039 (2016).

[21] C. R. Cabrera, L. Tanzi, J. Sanz, B. Naylor, P. Thomas, P. Cheiney, and L. Tarruell, Science **359**, 301 (2018).

[22] P. Cheiney, C. R. Cabrera, J. Sanz, B. Naylor, L. Tanzi, and L. Tarruell, Phys. Rev. Lett. **120**, 135301 (2018).

[23] G. Semeghini, G. Ferioli, L. Masi, C. Mazzinghi, L. Wolswijk, F. Minardi, M. Modugno, G. Modugno,

M. Inguscio, and M. Fattori, Phys. Rev. Lett. **120**, 235301 (2018).
[24] D. Anderson, A. Bondeson, and M. Lisak, J. Plasma Phys. **21**, 259 (1979).
[25] D. Anderson and M. Bonnedal, Phys. Fluids **22**, 105 (1979).
[26] D. Anderson, Phys. Rev. A **27**, 3135 (1983).
[27] D. Anderson, M. Lisak, and T. Reichel, J. Opt. Soc. Am. B **5**, 207 (1988).
[28] B. A. Malomed, Prog. Opt. **43**, 71 (2002).
[29] G. Fibich and A. L. Gaeta, Opt. Lett. **25**, 335 (2000).
[30] D. A. Steck, Rubidium 85 D Line Data, available at http://steck.us/alkalidata (2021), revision 2.2.3.
[31] R. Grimm, M. Weidemüller, and Y. B. Ovchinnikov, Adv. At. Mol. Opt. Phys. **42**, 95 (2000).
[32] C. J. Pethick and H. Smith, *Bose-Einstein Condensation in Dilute Gases*, 2nd ed. (Cambridge University Press, Cambridge, 2008).
[33] A. Cappellaro, T. Macrì, G. F. Bertacco, and L. Salasnich, Sci. Rep. **7**, 13358 (2017).
[34] A. Cappellaro, T. Macrì, and L. Salasnich, Phys. Rev. A **97**, 053623 (2018).
[35] H. Hu and X.-J. Liu, Phys. Rev. A **102**, 053303 (2020).
[36] H. Michinel, J. Campo-Táboas, R. García-Fernández, J. R. Salgueiro, and M. L. Quiroga-Teixeiro, Phys. Rev. E **65**, 066604 (2002).
[37] A. Alexandrescu, H. Michinel, and V. M. Pérez-García, Phys. Rev. A **79**, 013833 (2009).
[38] A. Paredes, D. Feijoo, and H. Michinel, Phys. Rev. Lett. **112**, 173901 (2014).
[39] H. Michinel, M. J. Paz-Alonso, and V. M. Pérez-García, Phys. Rev. Lett. **96**, 023903 (2006).
[40] N. Westerberg, K. E. Wilson, C. W. Duncan, D. Faccio, E. M. Wright, P. Öhberg, and M. Valiente, Phys. Rev. A **98**, 053835 (2018).
[41] K. E. Wilson, N. Westerberg, M. Valiente, C. W. Duncan, E. M. Wright, P. Öhberg, and D. Faccio, Phys. Rev. Lett. **121**, 133903 (2018).
[42] N. G. Vakhitov and A. A. Kolokolov, Radiophys. Quantum Electron. **16**, 783 (1973).
[43] J. J. Rasmussen and K. Rypdal, Phys. Scr. **33**, 481 (1986).
[44] G. Fibich, *The Nonlinear Schrödinger Equation: Singular Solutions and Optical Collapse*, Applied Mathematical Sciences Vol. 192 (Springer, Cham, 2015).
[45] H. A. Haus, Appl. Phys. Lett. **8**, 128 (1966).
[46] Z. K. Yankauskas, Sov. Radiophys. **9**, 261 (1966).
[47] R. Y. Chiao, E. Garmire, and C. H. Townes, Phys. Rev. Lett. **13**, 479 (1964).
[48] E. A. Donley, N. R. Claussen, S. L. Cornish, J. L. Roberts, E. A. Cornell, and C. E. Wieman, Nature (London) **412**, 295 (2001).
[49] L. Khaykovich, F. Schreck, G. Ferrari, T. Bourdel, J. Cubizolles, L. D. Carr, Y. Castin, and C. Salomon, Science **296**, 1290 (2002).
[50] K. E. Strecker, G. B. Partridge, A. G. Truscott, and R. G. Hulet, Nature (London) **417**, 150 (2002).
[51] C. Eigen, A. L. Gaunt, A. Suleymanzade, N. Navon, Z. Hadzibabic, and R. P. Smith, Phys. Rev. X **6**, 041058 (2016).
[52] M. I. Weinstein, Commun. Math. Phys. **87**, 567 (1983).
[53] P. Azam, Fluides quantiques de lumière avec des vapeurs atomiques chaudes, Ph.D. thesis, Université Côte d'Azur, 2021.
[54] K. D. Moll, A. L. Gaeta, and G. Fibich, Phys. Rev. Lett. **90**, 203902 (2003).
[55] B. Bakkali-Hassani, C. Maury, Y.-Q. Zou, E. Le Cerf, R. Saint-Jalm, P. C. M. Castilho, S. Nascimbene, J. Dalibard, and J. Beugnon, Phys. Rev. Lett. **127**, 023603 (2021).
[56] C.-A. Chen and C.-L. Hung, Phys. Rev. Lett. **125**, 250401 (2020).
[57] C.-A. Chen and C.-L. Hung, Phys. Rev. Lett. **127**, 023604 (2021).
[58] L. Bergé, Phys. Rep. **303**, 259 (1998).
[59] G. Ferioli, G. Semeghini, S. Terradas-Briansó, L. Masi, M. Fattori, and M. Modugno, Phys. Rev. Res. **2**, 013269 (2020).
[60] S. R. Otajonov, E. N. Tsoy, and F. K. Abdullaev, Phys. Rev. E **102**, 062217 (2020).
[61] P. Stürmer, M. N. Tengstrand, R. Sachdeva, and S. M. Reimann, Phys. Rev. A **103**, 053302 (2021).
[62] C. Fort and M. Modugno, Appl. Sci. **11**, 866 (2021).
[63] G. Labeyrie and U. Bortolozzo, Opt. Lett. **36**, 2158 (2011).
[64] Y. Silberberg, Opt. Lett. **15**, 1282 (1990).
[65] N. N. Akhmediev, V. I. Korneev, and R. F. Nabiev, Opt. Lett. **17**, 393 (1992).
[66] F. Ripka, H. Kübler, R. Löw, and T. Pfau, Science **362**, 446 (2018).
[67] Z. Bai, C. S. Adams, G. Huang, and W. Li, Phys. Rev. Lett. **125**, 263605 (2020).
[68] N. Defenu, T. Donner, T. Macrì, G. Pagano, S. Ruffo, and A. Trombettoni, arXiv:2109.01063.
[69] L. Chomaz, I. Ferrier-Barbut, F. Ferlaino, B. Laburthe-Tolra, B. L. Lev, and T. Pfau, Rep. Prog. Phys. **86**, 026401 (2023).
[70] F. Cinti, A. Cappellaro, L. Salasnich, and T. Macrì, Phys. Rev. Lett. **119**, 215302 (2017).
[71] T. Macrì, S. Saccani, and F. Cinti, J. Low Temp. Phys. **177**, 59 (2014).
[72] F. Cinti, T. Macrì, W. Lechner, G. Pupillo, and T. Pohl, Nat. Commun. **5**, 3235 (2014).
[73] T. Macrì and T. Pohl, Phys. Rev. A **89**, 011402(R) (2014).
[74] D. Laghi, T. Macrì, and A. Trombettoni, Phys. Rev. A **96**, 043605 (2017).
[75] F. Maucher, T. Pohl, S. Skupin, and W. Krolikowski, Phys. Rev. Lett. **116**, 163902 (2016).
[76] F. Maucher, N. Henkel, M. Saffman, W. Królikowski, S. Skupin, and T. Pohl, Phys. Rev. Lett. **106**, 170401 (2011).
[77] B. Bakkali-Hassani, C. Maury, S. Stringari, S. Nascimbene, J. Dalibard, and J. Beugnon, New J. Phys. **25**, 013007 (2023).
[78] G. R. Dennis, J. J. Hope, and M. T. Johnsson, Comput. Phys. Commun. **184**, 201 (2013).